Mass Transport in a Novel Two-Fluid Taylor Vortex Extractor

Gretchen Baier, Michael D. Graham, and Edwin N. Lightfoot
Dept. of Chemical Engineering, University of Wisconsin-Madison, Madison, WI 53706

Flow instabilities occurring in rotating flows can be exploited as a new approach to liquid–liquid extraction. Two immiscible liquids are radially stratified by centrifugal force in the annulus between corotating coaxial cylinders. When the inner cylinder is rotated above a critical speed, Taylor vortices form in one or both of the fluids. Although the flow pattern yields a relatively small amount of interfacial surface area, the surface is highly active for interphase mass transfer due to the local vortex motion. By adding countercurrent axial flow, efficient continuous processing is also possible. This flow yields a viable extraction process, particularly for fluid pairs that are easily emulsifiable and therefore have limited processing options with the current equipment commercially available. This article demonstrates that two-fluid Taylor-Couette flow with countercurrent axial flow is achievable in practice and explores, experimentally and computationally, the mass-transfer characteristics of the flow. Experimentally, when the vortices first appear, axial dispersion decreases and the interphase mass transfer starts to increase. Upon further increase in differential rotation rate, the extraction performance continues to improve, with the mass-transfer coefficient proportional to the strength of Taylor vortices. This suggests that very high extraction efficiencies can be obtained with even larger relative rotation rates. Furthermore, mass-transfer boundary-layer theory, in combination with computational fluid dynamics, provides a reliable method for predicting the extraction performance.

Introduction

Taylor-Couette flow results from the centrifugally induced hydrodynamic instability of flow between coaxial cylinders when the inner cylinder is rotated above a critical speed. Since Taylor's pioneering paper in 1923, this flow has attracted a great deal of study. Nevertheless, the extension to flow of two liquid phases in the same geometry has received relatively little attention. Here we study the mass-transfer characteristics of radially stratified two-fluid Taylor-Couette flow in an effort to develop a new device for liquid–liquid extraction. In a two-fluid Taylor-Couette extractor, the two phases retain their individual integrity and contact each other only at a single well-defined interface. Although the interfacial area is small, the vortex motion provides an active surface for mass transfer. This differs from the standard liquid–liquid extraction processes, which maximize a relatively inactive surface area by dispersing one phase as small droplets in the other phase. Such dispersion-based systems are often inadequate for liquid pairs that are easily emulsifiable, such as in bioseparations that use aqueous two-phase or reverse-micelle systems (Abbott and Hatton, 1988). Figure 1 depicts a two-fluid Taylor-Couette liquid extractor.

Taylor-Couette flow of a single fluid has already found applications that utilize the vortex motion to increase the performance of mass-transfer operations (Cohen and Marom, 1983; Holeschovsky and Cooney, 1991; Iosilevskii et al., 1993; Janes et al., 1987; Kroner et al., 1987; Kroner and Nissinen, 1988; Murase et al., 1991; Schechowskii et al., 1995). In many instances, a severalfold increase in filtration and reactor performance has been demonstrated (Cohen and Marom, 1983; Kroner et al., 1987; Kroner and Nissinen, 1988; Winzeler and Belfort, 1993; Belfort et al., 1993a,b). As a result, a number of researchers have experimentally and theoretically studied

Correspondence concerning this article should be addressed to E. N. Lightfoot.

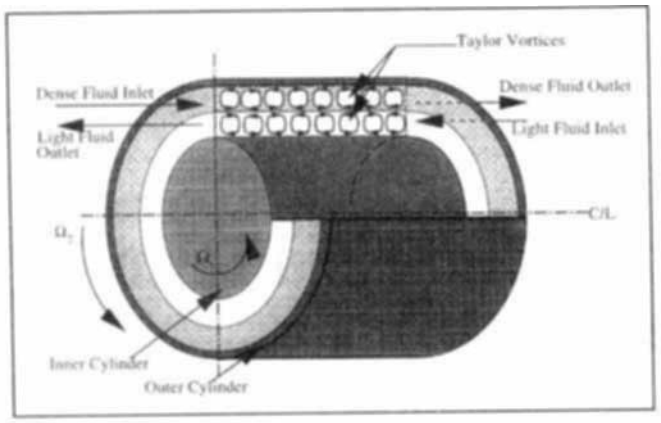

Figure 1. Two-fluid Taylor-Couette extractor.

the mass transfer in Taylor-Couette flow, including both axial transport (dispersion) and radial transport to or from a cylinder wall (Coeuret and Legrand, 1981; Holeschovsky and Cooney, 1991; Iosilevskii et al., 1993; Kataoka et al., 1975; Kataoka and Takigawa, 1981; Legrand et al., 1980; Moore and Cooney, 1995; Ohmura et al., 1997).

Experimental results for radial mass transfer in one fluid Taylor-Couette flow with a stationary outer cylinder approximately satisfy the relation

$$Nu_{\text{avg}} = ATa^{a}Sc^{b}, \tag{1}$$

where $Nu = 2kd/D$.

$$Ta = \frac{\Omega_1 R_1 d}{\nu}\left(\frac{d}{R_1}\right)^{1/2}, \quad Sc = \nu/D.$$

The radial mass-transfer coefficient is k, the inner and outer cylinder radii R_1 and R_2, the gap width $d = R_2 - R_1$, the diffusion coefficient D, the rotation rate of the inner cylinder Ω_1, and the kinematic viscosity $\nu = \mu/\rho$. The majority of the experiments conclude that $A = 0.4$–0.9, $a = 1/2$, and $b = 1/3$ (Coeuret and Legrand, 1981; Cohen and Marom, 1983; Flower et al., 1969; Holeschovsky and Cooney, 1991; Macleod and Ruess, 1975; Strong and Carlucci, 1976). Similar results are reported for Dean vortices in a helical tube (Gehlert et al., 1999). The Schmidt number dependence immediately suggests that the mass transfer is controlled by a boundary layer. Experiments have also shown that the mass transfer increases with increasing surface roughness (Grifoll et al., 1986; Kappesser et al., 1971), which is also consistent with boundary-layer theory where accelerated breakup of the boundary layer could increase the mass transfer. An axial Reynolds number, $Re_{ax} = \overline{W}d/\nu$, dependence can also appear in the Nusselt number relation, but this effect is observed only at high Reynolds numbers ($Re_{ax} > 300$), where the axial flow also significantly affects the critical Taylor number (Coeuret and Legrand, 1981; Simmers and Coney, 1979).

Almost all theoretical studies have relied on approximations or empirical parameters. A weakly nonlinear stability analysis of Taylor-Couette flow predicts that the axial velocity gradient is proportional to the just-defined Taylor number (Davey, 1962). From boundary-layer theory, the Nusselt number is then proportional to the Taylor number to the two-thirds power. This agrees surprisingly well with the experimental observations of one-half, considering that the weakly nonlinear analysis is valid only near the onset of the instability, which is not typically the region of experimental interest. Gu and Fahidy (1985) also apply boundary-layer theory, but used a parameter to fit the boundary-layer equations with the experimental results. Kawase and Ulbrecht (1988) provide insight into the mass-transfer characteristics of Taylor-Couette flow by comparing the numerical solution of mass transfer in a helical tube with published experimental results for Taylor-Couette flow. Flower and Macleod (1969) propose a basis for a "Large Vortex Model," claiming the mass and momentum transport analogy is not valid for Taylor-Couette flow due to the dissimilar boundary conditions. Similarly, Eisenberg et al. (1955) compare their experimental results with the Chilton-Colburn relation, and Simmers and Coney (1979) evaluate an analogy between heat and momentum transport.

Baier et al. (1999) have demonstrated that the experimental results can be accurately predicted without empiricism by using a combination of computational fluid dynamics (CFD) and boundary-layer theory. They calculate that $Nu \propto Ta^{0.46}$, which agrees well with the experimental exponents of 1/2 for Taylor-Couette flow as well as experiments in other systems with laminar boundary layers. The predicted amplitude is also in agreement with the highest predicted Nusselt numbers and is within a factor of 3 of the most of the experimental results, which include a wide range of geometries, systems, and measuring techniques.

A number of researchers have also investigated the axial mass transport (or axial dispersion) in Taylor-Couette flow. The experimental observations for one fluid Taylor-Couette flow indicate that axial dispersion decreases to a minimum near the onset of Taylor vortices and increases as the Taylor number increases (Pudjiono et al., 1992; Pudjiono and Tavare, 1993). When axial flow is not present, the dispersion is proportional to the square root of the diffusion coefficient (Desmet et al., 1996b), but when axial flow is present, the dispersion is independent of the diffusion coefficient (Moore and Cooney, 1995; Giordano et al., 1998) and increases with increasing axial flow rates (Enokida et al., 1989; Moore and Cooney, 1995). These experimental results have been modeled as one-dimensional convection-diffusion plug flow (Enokida et al., 1989; Moore and Cooney, 1995; Tam and Swinney, 1987) or as a mixing-tanks-in-series system (Kataoka et al., 1975; Legrand et al., 1980). One research group has combined the plug-flow and mixing-tank models into a single overall model correlating the axial mass transfer to the position in the vortex (Desmet et al., 1996a,b). Convection dominates near the vortex boundaries and diffusion dominates near the center of the vortex.

The corresponding theoretical work for predicting axial dispersion in one fluid Taylor-Couette flow has included asymptotic and full numerical analyses. Rosenbluth et al., (1987) present results for axisymmetric Taylor-Couette flow without axial flow in an infinitely long annulus in both the high and low Peclet (Pe) number limits. When $Pe \ll 1$, the vortex is of almost uniform composition. In this case, Rosenbluth et al. (1987) find that $D^* \propto DPe^2$. This relationship is the same as for Taylor-Aris convective dispersion (Taylor,

1953; Aris, 1956). When $Pe \gg 1$, the effect of diffusion is small and boundary layers form along the vortex boundaries with little diffusion into the interior of the cell. It is this limit that is typically observed experimentally. Rosenbluth et al. (1987) find in this limit that $D^* = cDPe^{1/2} = c(Dud)^{1/2}$, where u is the characteristic flow velocity in a convective cell. The constant c is dependent on the system geometry and the flow velocity at the cell boundary. The dependence of the dispersion coefficient on the square root of the Peclet number reflects the existence of mass-transfer boundary layers at the cell boundaries. From a weakly nonlinear stability analysis (Davey, 1962), $u \propto Re_\theta$, which leads to the boundary-layer theory relation $D^* \propto Re_\theta(Sc)^{1/2}$. This equation compares favorably with the experimental observations $D^* \propto Re_\theta^a$, where typically $0.69 < a < 1.05$. This agreement is somewhat surprising since the weakly nonlinear analysis is strictly valid only near the onset of the vortex flow, whereas the experiments were generally nearer the turbulent vortex regime.

When axial flow is present, the theoretical analysis of axial dispersion in Taylor-Couette flow becomes much more complicated. In Taylor-Couette flow with axial flow, some streamlines (in a reference frame moving with the wave speed) bypass the vortices and the wave speed is higher than the mean axial flow velocity, $\overline{W}$ (Chandrasekhar, 1961; Howes and Rudman, 1998). To calculate the long-time dispersion coefficient, Howes and Rudman use the method of moments developed by Brenner (1980). They assume that the dispersion can be described by two terms: (1) the vortex boundary transport, where $D^* \propto D^{1/2}$, and (2) the axial transport due to axial flow, where $D^* \propto \overline{W}^2 d^2/D$. Experimentally, increasing the axial flow rate does increase the axial dispersion, but with a weaker dependence than predicted here. This discrepancy may be a result of the assumptions of long-time and axisymmetry in the theoretical analysis of Howes and Rudman (1998). They did not study the effect of azimuthal Reynolds number on the axial dispersion, so the initial decrease and subsequent increase in dispersion is currently not understood.

When penetration theory and computational fluid dynamics are used to predict axial dispersion in Taylor-Couette flow without axial flow, the trends are again clear that increasing vortex strength increases axial dispersion. However, the magnitude of the calculated dispersion coefficient is an order of magnitude lower than the experimental values. Moore and Cooney (1995) also observed a large discrepancy when comparing their experimental results with Rosenbluth's predictions. The experiments included axial flow, while the theory did not, and this discrepancy indicates the importance of convective transport. Furthermore, Moore and Cooney found that a change in the Schmidt number by two orders of magnitude did not effect axial dispersion. This is in conflict with all of the theoretical models and further highlights the complex nature of axial dispersion. In summary, although the qualitative trends are consistently observed and predicted, the quantitative dependence of the dispersion on the azimuthal Reynolds number and axial Reynolds number varies widely.

In this article, we present the mass-transfer characteristics of two-fluid Taylor-Couette flow. This includes experimental results for axial dispersion (intraphase mass transfer) in both phases and radial mass transfer (interphase mass transfer or extraction) across the interface. Furthermore, a combination of boundary-layer theory and CFD is used to predict theoretically the interphase mass transfer without empiricism. The experiments and theory agree quite well and indicate that two-fluid Taylor-Couette is a promising liquid extraction process. In addition, boundary-layer theory and CFD provide reliable predictions with which to design an optimized two-fluid Taylor-Couette extractor.

Fluid Mechanics

Inviscid analysis

The fluid mechanics of two-fluid Taylor-Couette flow are well understood in the regime of interest here, and have been presented in companion papers (Baier and Graham, 1998, 2000). The basic features of two-fluid Taylor-Couette flow are revealed in the following inviscid analysis. When the annulus is filled with a single inviscid fluid in purely azimuthal motion, Rayleigh argued on physical grounds and Synge showed rigorously that the flow is unstable if the square of the angular momentum decreases with increasing radial position anywhere in the domain (Drazin and Reid, 1981). For Couette flow, this "Rayleigh criterion" can be written, in terms of experimentally controllable parameters, as $\Omega_{21} < R_{12}^2$. The outer cylinder has radius R_2 and rotates with angular velocity Ω_2, and similarly for the inner cylinder. The cylinder rotation-rate ratio is then $\Omega_{21} = \Omega_2/\Omega_1$ and the radius ratio $R_{12} = R_1/R_2$. The effect of viscosity is stabilizing and therefore the Rayleigh criterion is a necessary condition for Taylor-Couette flow and is an asymptote approached as viscous effects vanish.

In the corresponding inviscid analysis for two-fluid Taylor-Couette flow without countercurrent flow, each fluid layer is considered to be inviscid, but with the base Couette flow-velocity profile, so although this is an inviscid analysis, the viscosity *ratio* remains important because it determines the velocity profile. Each phase is then subject to a Rayleigh criterion similar to that for the one fluid case (Baier and Graham, 1998). According to this criterion, instability occurs in the inner fluid when Ω_{21} is less than a critical value $\Omega_{21,c,1}$ with

$$\Omega_{21,c,1} = \frac{R_{12}^2 + (\mu_{21} - 1)R_{1i}^2}{\mu_{21}}, \tag{2}$$

and in the outer fluid when

$$\Omega_{21} < \Omega_{21,c,2} = \frac{R_{12}^2}{\mu_{21} - (\mu_{21} - 1)R_{1i}^2}. \tag{3}$$

Here the interface is located at R_i and rotates at Ω_i; the inner fluid (fluid 1) has viscosity μ_1, which is similar for the outer fluid, so the viscosity ratio is $\mu_{21} = \mu_2/\mu_1$. These Rayleigh criteria predict that for a given interface position, the less viscous fluid is always the one more susceptible to instability. When viscous effects are important the analysis is more complex, but for equal fluid depths the Rayleigh criterion accurately predicts the unstable phase. For sufficiently small values of $\mu/(\rho\Omega_2 d^2)$, the fluids behave as if they were inviscid and the Rayleigh criterion agrees quantitatively with experiments. Figure 2 shows several stream functions for var-

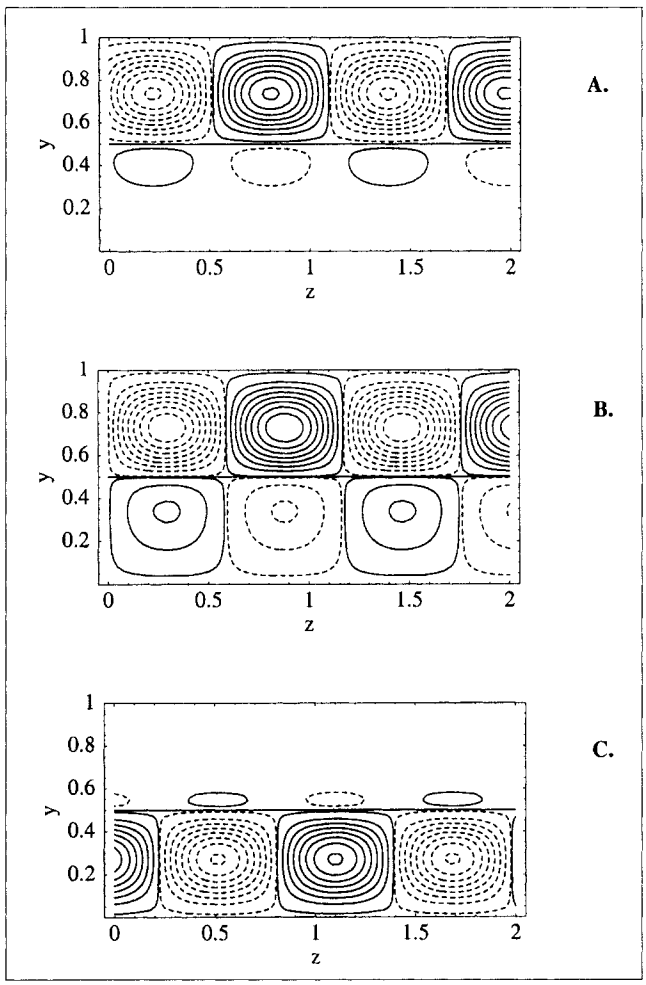

Figure 2. Stream function for two-fluid Taylor-Couette flow with various viscosity ratios.

Here $y = (r - R_1)/(R_2 - R_1)$, $\rho_{21} = 1.36$, $\rho_2 = 1.15$ g/mL, $R_{12} = 0.826$, $R_2 = 5.05$ cm, $\Omega_2 = 8$ rev/s, $\mu_2 = 7.5$ cp, $Q_1 = Q_2 = 0$, and equal fluid depths. The vortices represented by the solid lines rotate in the opposite direction to those represented by the dashed lines. (A) $\mu_{21} = 0.2$, $\Omega_{21} = \Omega_{21c} = 0.7955$; (B) $\mu_{21} = 1.0$, $\Omega_{21} = \Omega_{21c} = 0.6794$; (C) $\mu_{21} = 5.0$, $\Omega_{21} = \Omega_{21c} = 0.7908$.

ious viscosity ratios from the detailed viscous linear stability analysis (Baier and Graham, 1998). The vortex motion is stronger in the Rayleigh unstable phase and drives the vortex motion in the other phase.

Computational fluid dynamics

The linear stability analysis is useful for understanding the onset of the vortex flow, but does not predict behavior beyond the critical point. Therefore, the computational fluid dynamics package, FIDAP (Fluent, Inc., Evanston, IL), was used to calculate the velocities required in the boundary-layer analysis discussed below. FIDAP was chosen because it uses an adaptive finite-element mesh to accurately resolve the interface position. Our fluid mechanics studies (Baier and Graham, 1998, 2000) predict that with low axial flow rates the flow is axisymmetric near the onset of the vortices, so axisymmetry was assumed for the computations. Countercurrent axial flow was included in the CFD calculations by requiring the ends to have the countercurrent axial profile calculated analytically in the absence of vortices. In the FIDAP runs, the axial wavenumber is controlled by the aspect ratio. We impose length/gap width = 1, consistent with the theoretical predictions and experimental observations of vortex aspect ratios close to one (Baier and Graham, 1998, 2000). For comparison with the experimental data, the conditions (radii, viscosities, densities) for a CFD run were chosen to match the corresponding experiments. The FIDAP runs were started at rigid rotation (12.5 rev/s) with the analytical solution at rigid rotation as the initial condition. The outer cylinder rotation rate was then continuously decreased to its final value. The results presented are for solutions where the transient behavior has ceased to be important. Furthermore, wave number multiplicity is forbidden by the choice of boundary conditions. Near the cylinder walls and interface a fine grid was used, with a gradual coarsening toward the center of each fluid region. Near the onset of the vortex flow, FIDAP predicts a flat interface, which deforms upon further increases past the critical point. This agrees with the experimental observations and linear theory (Baier and Graham, 1998). The point of maximum interface deformation occurs where the flow is directed radially toward the interface in the Rayleigh unstable phase; the layer depth of that unstable phase is the greatest at this point. For a given outer phase viscosity, the interface deformation increases with increasing viscosity difference between the two phases.

The primary purpose of the FIDAP calculations is to provide the velocity field for use in the boundary-layer equations. However, during the course of the CFD study an interesting and counterintuitive feature of two-fluid Taylor-Couette flow was also observed. Without countercurrent axial flow, FIDAP predicts that at sufficiently high Taylor numbers, vortex pairs across the interface *corotate* with each other. Figure 3 includes the FIDAP stream functions for counter- and corotating vortices. This corotation is not an effect of interface deformation, but results from a secondary branch that bifurcates from the Couette flow solution and becomes stable only at higher relative rotation rates. For corotating vortices, poorer mass-transfer performance would be expected: $Nu \propto Pe^{1/3}$ instead of $Nu \propto Pe^{1/2}$, as discussed below. Corotation of vortices paired across the interface of axially stratified two-fluid Taylor-Couette flow was also observed by Toya and Nakamura (1997). When countercurrent axial flow is present, FIDAP does not predict corotating vortices, which is consistent with the fluid mechanics analysis presented elsewhere (Baier and Graham, 2000).

Boundary-layer theory

In general it can be quite difficult to accurately calculate mass-transfer coefficients. Real systems are often complex and include physical property gradients, convective dispersion, and complicated geometries. Fortunately, in many situations the majority of mass transfer is limited to a thin boundary-layer region. In this case, boundary-layer theory provides analytical solutions that can be very accurate and are much less cumbersome than a full numerical analysis, which requires very high numerical resolution in the boundary-layer region. Typically, boundary-layer theory is useful under the

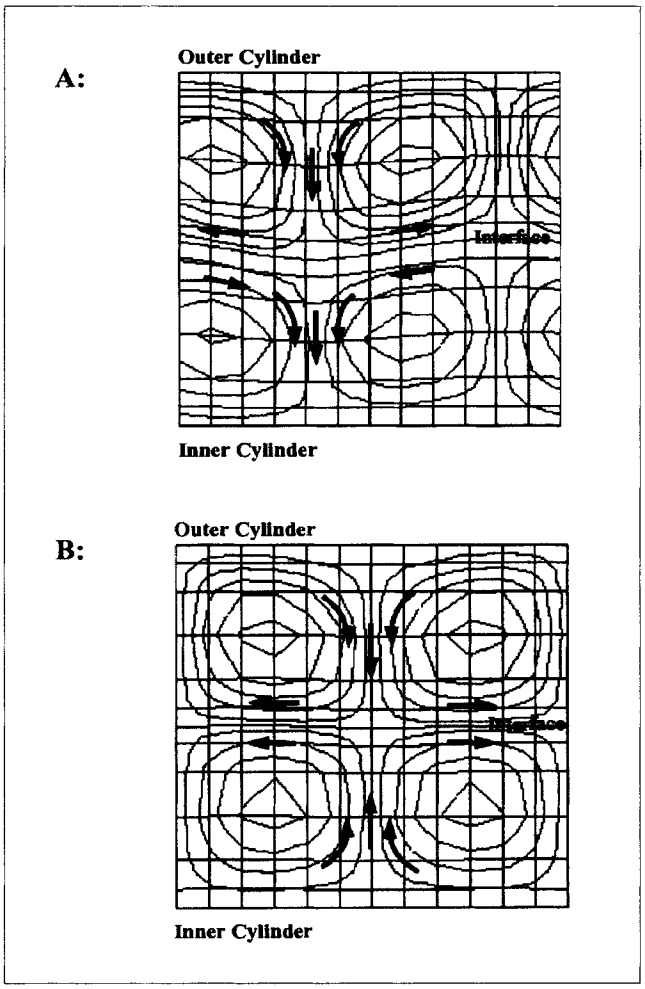

Figure 3. FIDAP stream function results for 60 wt. % glycerine in water and 50 wt. % Drakeol-35 in IsoPar-L ($\mu_{21} = 0.96$, $\Omega_{21} = 0.62$).

(A) Without axial flow, the vortices corotate across the interface and the interface deformation is significant. (B) With axial flow ($Re_{ax,2} = 0.33$), the vortices counterrotate across the interface and the interface deformation is small.

following conditions: (1) the Schmidt number is sufficiently large that the concentration boundary-layer thickness is small compared to both the velocity boundary layer and the local radius of curvature of the boundary; (2) the velocity in the concentration boundary layer is nearly parallel to the surface; (3) diffusion in the direction of the flow is negligible ($\partial^2 C/\partial z^2 \ll \partial^2 C/\partial y^2$, where y and z represent the directions normal and tangent to the mass-transfer surface, respectively); (4) the concentration gradient is primarily confined to the concentration boundary layer; (5) the physical properties are constant; and (6) in periodic flows, the fluid from the boundary-layer region is mixed with the bulk fluid by the time the period is complete.

When the concentration boundary layer is thin compared to the velocity boundary layer, the velocity profile within the concentration boundary layer may be approximated either as (1) a linear profile, to approximate mass transfer from a solid surface such as flow past a flat plate, or as (2) a flat profile, to approximate the mass transfer across a fluid–fluid interface such as a falling film. The analysis with this flat velocity profile approximation is often referred to as penetration theory. To use boundary-layer theory, only the velocity gradient or the velocity at the mass-transfer surface is required, depending on the approximation used. In only a few cases is this velocity information obtainable analytically, and in general numerical methods as discussed earlier are required to determine the velocity field.

The general two-dimensional boundary-layer solution (for dilute solutions in laminar flow) was developed by Acrivos (1962) and extended to three dimensions by Stewart (1963). For the linear profile approximation, the local Nusselt number is defined as (Lightfoot, 1969)

$$Nu_{\text{loc}}(z) = \frac{(ReSc)^{1/3}}{9^{1/3}\Gamma(4/3)} \frac{\sqrt{\dot{\gamma}(z)}}{\left[\int_{z_0}^{z} \sqrt{\dot{\gamma}(s)}\, ds\right]^{1/3}} = g(\text{geometry}, Re) Re^{c} Sc^{1/3}, \quad (4)$$

where Re is the Reynolds number and $\dot{\gamma} = \partial v_z/\partial y$ the velocity gradient at the mass-transfer surface. The function g is typically only weakly dependent on the Reynolds number and is often taken to be independent of it. The Reynolds number exponent, c, depends on the flow conditions and is 1/3 for creeping flows ($Re \ll 1$) and 1/2 for most laminar boundary-layer flow systems ($Re \gg 1$).

For the flat profile approximation, the local Nusselt number is defined as (Lightfoot, 1969)

$$Nu_{\text{loc}} = \left(\frac{ReSc}{\pi}\right)^{1/2} \frac{u_0(z)}{\left[\int_{z_0}^{z} u_0(s)\, ds\right]^{1/2}} = h(\text{geometry}, Re) Re^{c} Sc^{1/2}, \quad (5)$$

where u_0 is the velocity tangential to the interface. The function h is again typically only a weak function of the Reynolds number and is often taken to be independent of it.

The average Nusselt number, Nu_{avg}, is found by integrating the local Nusselt number over the desired length and dividing by that length. Since Taylor-Couette flow is periodic, the desired length here is the width of one vortex, which is approximately the gap width, since the vortices are approximately square. The boundary layer begins to form at z_0, which is a vortex boundary. Furthermore, since the flow is symmetric, the average Nusselt number for a vortex with clockwise rotation is equal to that of its axial neighbor with counterclockwise rotation. The flat profile approximation (penetration theory) is used in the analysis for counterrotating vortices (cocurrent flow at the interface) and the linear profile approximation for corotating vortices (countercurrent flow at the interface). Since the interface is free to deform, the velocity component tangential to the interface was calculated from the FIDAP results and used in the boundary-layer analysis; the normal component was confirmed to be zero. The Peclet number is consistent with the scaling in the linear stability analysis $Pe = ReSc = \Omega_1 R_1 d/D_2$ (Baier and Graham, 2000).

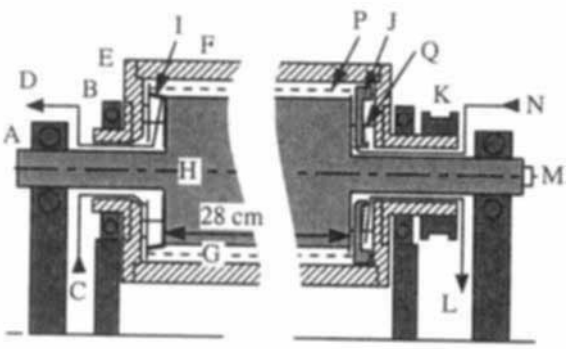

A – Inner cylinder pillow block bearing
B – Outer cylinder bearing
C – Heavy fluid inlet
D – Light fluid outlet
E – Plexiglas endplate with removable windows
F – Plexiglas outer cylinder, $R_2 = 5.05$ cm
G – 0.88 cm fluid filled gap
H – Stainless steel inner cylinder, $R_1 = 4.17$ cm
I – Underflow weir
J – Overflow weir
K – Flat belt coupling to outer cylinder motor
L – Heavy fluid outlet
M – Direct coupled inner cylinder motor
N – Light fluid inlet
P – Fluid–fluid interface
Q – Fluid–air interface

Figure 4. Equipment design with the weir system.

Experimental Design

Equipment design

The experimental apparatus, illustrated in Figure 4, consists of a pair of horizontal coaxial cylinders with a weir system at the ends for countercurrent flow. The fluids must be added or removed from the annulus while the cylinders rotate at a speed sufficient for centrifugal stratification, thus in effect creating an air seal. The sealless design offers the advantages of mechanical simplicity and easy access to the fluid-filled annulus. The disadvantage is that experiments with very slowly rotating cylinders are not possible. This type of operation, however, is not of interest here.

The inner- and outer-cylinder rotation rates are independently controlled by two Compumotor stepper motors and drivers (Triphase Automation, Waukesha, WI). The larger motor (OEM-83-62) is direct coupled to the inner cylinder, and the smaller motor (OEM-57-83) belt drives the outer cylinder. The motors are powered in series and controlled through two Compumotor OEM650X-M2-RC drivers with position controllers (25,000 steps/rev). The drivers are controlled from a PowerMac through a Zterm interface.

The outer cylinder is cast Plexiglas with inner diameter 10.098 ± 0.008 cm, and the inner cylinder is stainless steel with diameter 8.349 ± 0.003 cm. The coaxial alignment of the two cylinders was measured and optimized through small removable, liquid-tight windows in the endplates attached to the outer cylinder. A telescoping gauge and micrometer were used to measure the gap thickness at three locations on each end. The measurement of the alignment is possible only without the weirs and is assumed to be representative with the weirs. The alignment of the two cylinders is such that the gap on either end is 0.882 ± 0.017 cm ($\pm 2\%$). This variation in the gap width is not expected to have a significant effect on the flow field based on the one-fluid analog (Koschmieder, 1976; Versteegen and Jankowski, 1969). The length of the annulus is $L = 29.5$ cm for an aspect ratio of $L/d = 33.5$.

A wide variety of weir configurations was evaluated in an effort to reduce end effects. When the cylinders rotate at different speeds, structures that are attached to the inner cylinder (1) are coated with a film of inner fluid, and (2) provide strong outward radial pumping action of the inner fluid that can strongly affect the interface position. In contrast, structures that are attached to the outer cylinder introduce an opposite effect and outer fluid can be drawn radially inward. Ultimately, the weir configuration illustrated in Figure 4 was chosen. The inner-fluid-feed/outer-fluid-withdrawal weir consists of:

1. An outer-fluid overflow weir attached to the outer cylinder. When this weir is attached to the inner cylinder, the previously mentioned pumping action causes inner-fluid carryover into the outer-fluid withdrawal stream.
2. A small plate attached to the inner cylinder that has a slightly larger diameter than the inner cylinder. The plate diameter controls the interface position at this end and inner-fluid feed is introduced against this plate.

The outer-fluid-feed/inner-fluid-withdrawal weir consists of:

1. A plate attached to the outer cylinder that has a slightly smaller diameter than the outer cylinder. Outer fluid is introduced against this plate. When this plate is attached to the inner cylinder, the resulting pumping action can cause inner-fluid carryover into the outer-fluid feed reservoir and severe mixing.
2. An underflow weir attached to the inner cylinder. This weir is a modified *N*-buna flared piston cup that also acts as a crude rotary seal against the outer-fluid plate to prevent outer fluid that is drawn radially inward from entering the inner-fluid outlet reservoir.

The apparatus remains horizontal and the axial counterflow is driven by the axial pressure drop for the respective phase. As a result, the interface is slightly tapered rather than cylindrical. A perturbation analysis reveals that at rigid rotation (i.e., $\Omega_1 = \Omega_2$) the taper is approximately

$$\frac{\delta}{d} = \frac{1}{(1-\rho_{12})} \frac{LR_2}{d^2} \frac{Re_{ax,2}}{Re_2^2} \left(\mu_{12}^2 \rho_{21} \frac{Re_{ax,1}}{Re_{ax,2}} + 1 \right),$$

where $\delta + R_i$ is the maximum radius of the tapered interface (i.e., its radius at one end) and $Re_2 = \Omega_2 R_2 d/\nu_2$ (Baier and Graham, 2000). The taper increases with increasing axial flow or an increasing difference in the flow rates, but decreases with increasing centrifugal force (Re_2) or increasing density difference. For the results presented in this article, $\delta/d < 0.04$ with $L/R_2 = 5.55$.

In addition to the weir system, a bulk reservoir and pumping accessories were required for countercurrent axial flow. In order to maintain a steady-state interface position in the annulus, the inlet flow rate for each phase has to precisely match the outlet flow rate. For the aqueous phase this was

Table 1. Physical Properties of the Fluids Used in the Experiments*

Pair	Nominal Wt. % Glycerine	Nominal Wt. % Drakeol-35	μ_2 (cp)	ρ_2 (g/mL)	μ_{21}	ρ_{21}
1	60	60	7.52	1.15	0.63	1.40
2	60	50	7.52	1.15	0.96	1.40
3	60	40	7.52	1.15	1.46	1.43

*Percentages refer to the corresponding phase, for example, for fluid pair 1 the aqueous phase is 60% glycerine and the organic phase 60% Drakeol-35. Phase 2 is always the outer (more dense, aqueous) phase.

accomplished by using a reservoir system consisting of a collection bag contained in a large flask. As the aqueous outlet flow was collected in the bag, the bag expanded and caused fresh fluid surrounding the bag out of the flask, thus providing an inlet flow that is matched to the outlet flow rate. For the organic phase, however, the collection bag system was abandoned, because the organic phase would leach plasticizer from the bag, interfering with the UV measurements. Instead, a two-flask system was used with an aqueous seal fluid. For the same reason, the organic fluids were stored in glass or coated metal containers, and special Tygon (F-4040-A) or Viton tubing was used for all of the inner-fluid lines.

The pumping system was further simplified by only considering equal flow rates of the inner and outer fluids. Therefore only one Masterflex peristaltic pump was required with two coupled pump heads (one for each phase). The flow rates were calibrated and controlled by the rotation rate of the pump head.

Fluids used in the experiments

The physical properties of the fluids investigated are summarized in Table 1. The aqueous phase was glycerine in water, and the organic phase was white mineral oil (Drakeol-35, Superior Lubricants, Tonawonda, NY) in a hydrotreated petroleum distillate (Isopar-L, Famous Lubricants, Chicago, IL). The kinematic viscosities were measured at 25°C on a Schott Geräte capillary viscometer calibrated with sucrose solutions. The densities were measured at room temperature on an Aton Parr DMA40 digital density meter calibrated with water and air. The dynamic viscosity ($\mu = \nu\rho$) was calculated from the measured values for density (ρ) and kinematic viscosity (ν).

Axial dispersion and extraction experimental design

For the mass-transfer experiments a tracer was injected into an inlet stream and the outlet streams monitored. The properties of the various tracers are summarized in Table 2. For the dispersion experiments, the tracer is soluble in only one phase. For the extraction experiments, the tracer is soluble in both phases, as defined by the partition coefficient

$$m = \frac{C_2^*}{C_1^*}, \tag{6}$$

where C_1^* and C_2^* are the equilibrium concentrations of the tracer in the inner and outer fluids (phases 1 and 2), respectively. The partition coefficient was measured spectroscopically and determined to be independent of the composition of the organic and aqueous phases for the ranges investigated. The outlet streams were both monitored with a Beckman DU65 UV-VIS Spectrophotometer using quartz flowthrough cells (Fisher Scientific) and a multisample scanning system. Upstream of the inner-fluid UV cell was a small knockout pot to prevent any small amount of outer-fluid carryover from collecting in the inner-fluid UV cell. The spectrophotometer was calibrated with standard samples of each tracer at the typical concentrations and flow rates of the experiments. The readings from the spectrophotometer were recorded to a PowerMac through a Kermit interface. Data analysis was done in Mathematica.

Table 2. Properties of the Tracers Used in the Dispersion and Extraction Experiments

Tracer	Partition Coeff., m	Exp.	Monitoring Wavelength (nm)
Acetophenone	0.125	Extraction	255
sec-Phenethyl alcohol	2.7	Extraction	255
Benzyl alcohol	14.0	Extraction	258
Sudan-IV	0	Dispersion	520
Amarath red	∞	Dispersion	520

For all of the mass-transfer experiments the volumes of the two phases were matched ($V_1 = V_2 = 4 \times 10^2$ mL). After each series of runs, the fluid volumes collected from the annulus were measured and determined to be within 10% of the initially loaded volume for each phase. Likewise, the volumetric flow rates were matched and were typically $Q_1 = Q_2 = 20$ mL/min, giving a 20-min average residence time, with $Re_{ax,2} = 0.33$. The inner-cylinder rotation rate, Ω_1, was constant at 12.5 rev/s, and the outer-cylinder rotation rate, Ω_2, was varied from 7.5 to 12.5 rev/s. Lower values of Ω_2 would result in emulsion formation at the ends, and therefore were not studied. In the parameter regime studied, the pattern that emerged as Ω_2 decreased always consisted of axisymmetric steady vortices with an aspect ratio very close to 1. In general, a traveling-wave pattern is expected in an unbounded geometry (Baier and Graham, 2000), but apparently the combination of matched flow rates and the boundary conditions at the ends of the device acted to "pin" the vortex pattern in place. No multiplicity or hysteresis were found with the experimental protocol used.

Axial Dispersion Experiments. Axial dispersion is characterized by the change in the tracer concentration curve from the inlet injection to the outlet response. When the injection of tracer is assumed to be an instantaneous pulse, as we tried to achieve in the experiments, the extent of axial dispersion is determined only by the shape of the outlet response curve, $C(t)$. This curve can be characterized by its moments:

$$M_0 = \int_0^\infty C(t)\, dt \tag{7}$$

$$M_1 = \frac{1}{M_0}\int_0^\infty tC(t)\, dt \tag{8}$$

$$M_2 = \frac{1}{M_0}\int_0^\infty (t - M_1)^2 C(t)\, dt. \tag{9}$$

The zeroth moment, M_0, is used for a mass balance on the tracer. The first moment, M_1, reflects the average residence time, and with the second central moment, M_2, determines the dispersion.

Several models are available to describe axial dispersion. The simplest continuous model is simply

$$\frac{\partial < C >}{\partial t} + \bar{W}\frac{\partial < C >}{\partial z} = D^* \frac{\partial^2 < C >}{\partial z^2},$$

where D^* is an empirical dispersion coefficient (Levenspiel, 1972), and the angle brackets denote averages across the fluid layer. This dispersion model is preferred when the outlet curves are Gaussian, since its impulse response is always Gaussian. Alternatively, the dispersion can be represented by a series-of-mixing-tanks model, with the extent of dispersion corresponding to the number of mixing tanks. The number of mixing tanks can be calculated by (Levenspiel, 1972)

$$N = \frac{M_1^2}{M_2}. \tag{10}$$

In this case, fewer mixing tanks indicate higher dispersion. The mixing-tank model better represents situations where the output is not Gaussian (Levenspiel, 1972). The mixing-tank model was used in our analysis, and Figure 5 shows typical outlet response curves for pulse input. The number of mixing tanks was determined by first fitting the outlet response data with a Fourier series to reduce the contribution of noise. This curve was then integrated to find the moments and to characterize the dispersion. The mass balance and the average residence time were typically within 10% of the expected values.

Extraction Experiments. The extraction experiments consisted of injecting a pulse of tracer into the inlet stream of one phase and measuring its concentration in the outlet streams of both phases. Typically the tracer was introduced into the inner fluid feed stream and was therefore premixed with inner fluid to provide a more homogeneous injection. Figure 6 shows a pair of typical outlet response curves for a pulse input. The extraction performance was determined by first fitting the outlet response data with a truncated Fourier series to reduce the contribution of noise. The two outlet

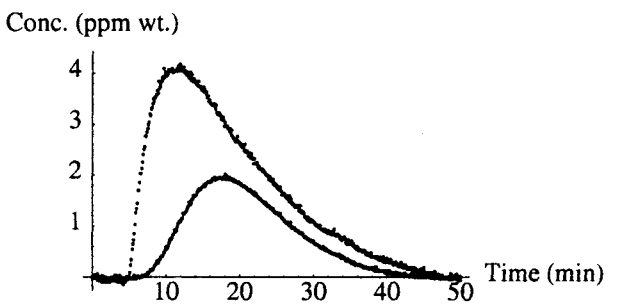

Figure 5. Typical outlet response curves for the axial dispersion experiments.

The more symmetric (lower) curve corresponds to a higher number of mixing tanks, and in this case, the inner fluid. The other curve is for the outer fluid. $\Omega_{21} = 0.696$, $\mu_{21} = 1.46$, $Re_{ax,2} = 0.33$, $N_1 = 8.8$, $N_2 = 4.5$.

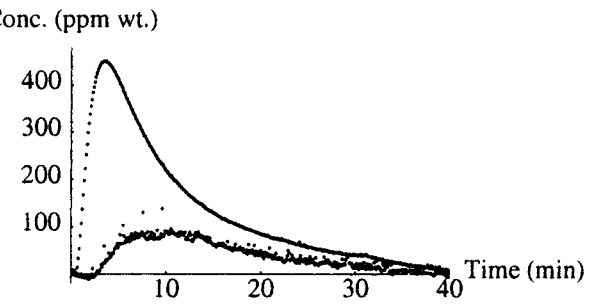

Figure 6. Typical outlet response curves for the extraction experiments.

The upper curve corresponds to the extract (outer) phase, the lower curve the raffinate (inner) phase. $\Omega_{21} = 0.6$, $\mu_{21} = 0.96$, $Re_{ax,2} = 0.33$, $m = 2.7$, $f = 0.78$, $Nu = 440$.

curves were then integrated to find the zeroth moment for each phase. A total mass balance and the percent of tracer extracted were then calculated. The error in the computed mass balance was typically less than 10% and the run-to-run variation in fraction extracted about $\pm 5\%$.

The overall mass-transfer coefficient can be defined by the one-dimensional differential mass-balance equation (Lo et al., 1983) along the length of the extractor

$$u_{z,1} dC_1(z) = (aK_1)\left[C_1^*(z) - C_1(z)\right] dz, \tag{11}$$

where $u_{z,1}$ is the linear velocity of the inner fluid, C_1 is the concentration in the inner fluid, C_1^* is the concentration in the inner fluid that would be in equilibrium with the concentration in the outer fluid (C_2), a is the mass-transfer surface area per unit volume, and K_1 is the overall mass-transfer coefficient based on the inner fluid. The mass-transfer area is usually unknown in systems that disperse one phase in the other. Here, however, we can accurately calculate our interfacial area per unit volume from the FIDAP runs. Since the interface deformation is small, the interfacial area may also be well estimated by assuming a cylindrical interface with radius R_i, so $a = 2R_i/(R_2^2 - R_1^2)$. This overall mass-transfer coefficient is related to the individual mass-transfer coefficients, which typically cannot be measured directly:

$$\frac{1}{K_1} = \frac{1}{k_1} + \frac{1}{mk_2}, \tag{12}$$

where k_1 and k_2 are the individual mass-transfer coefficients for the inner and outer fluids, respectively. This definition of the overall mass-transfer coefficient also includes the effects of dispersion; higher rates of dispersion result in lower overall mass-transfer coefficients. Equation 11 can be integrated to find the mass-transfer coefficient

$$aK_1 = \frac{u_{z,1} m}{(1-m)L} \ln \frac{(1-f)}{(1-f/m)}, \tag{13}$$

where f is the fraction extracted, as determined experimentally. The Nusselt number, Nu, is the dimensionless mass-transfer coefficient $Nu = K_1 d/D_2$.

The number of theoretical stages, n, is the number of equilibrium batch separations that would be required to obtain a given separation and is calculated from the equation

$$n = \frac{\ln \dfrac{E-f}{E(1-f)}}{\ln E} \tag{14}$$

where $E = mQ_2/Q_1$ and Q_1 and Q_2 are the volumetric flow rate of the inner and outer fluids, respectively (Treybal, 1963). The higher the number of theoretical stages, the better the separation.

Experimental Results

Axial dispersion

The effects of Taylor number and axial flow rates on mass transfer are expected to be similar in one- and two-fluid Taylor-Couette flow, as discussed in the Introduction. However, in the two-fluid case, axial dispersion must be considered for both phases. When only one phase is Rayleigh unstable, the boundary conditions require weak vortices in the other phase (Figure 2), and as a result axial dispersion is expected to decrease in both phases.

With the addition of countercurrent axial flow, however, the effects on axial dispersion are less predictable. Before the onset of vortices, the countercurrent axial velocity profiles can be easily determined by the equations of motion and continuity. When the fluid viscosities, axial flow rates, and the fluid depths of the two phases are not matched, backflow (i.e., flow against the pressure gradient, driven by the shear stress at the interphase boundary) can occur in one of the phases, leading to increased axial dispersion in that phase. Figure 7 illustrates the velocity profile for countercurrent axial flow and the resulting backflow. However, this backflow effect can be mitigated by the presence of Taylor vortices in that phase to reduce axial dispersion. For the countercurrent flow rates accessible in the experiments, the effect of Taylor vortices seems to dominate the effect of backflow, and axial dispersion is minimized near the onset of the vortex flow.

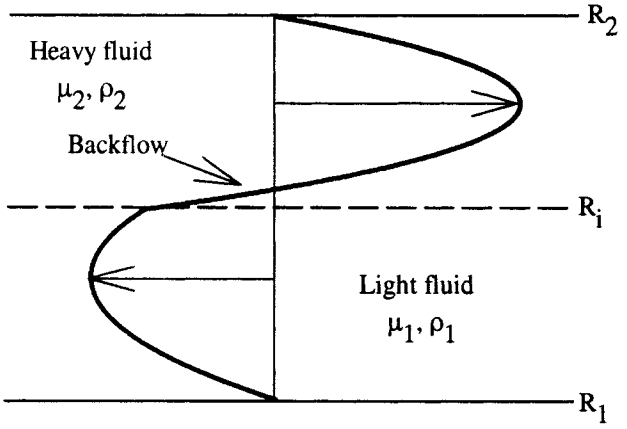

Figure 7. Velocity profile for the countercurrent axial base flow.

$R_{12} = 0.826$, $d/R_2 = 0.174$, $Q_1 = Q_2$, $\mu_{21} = 0.22$, and equal fluid depths.

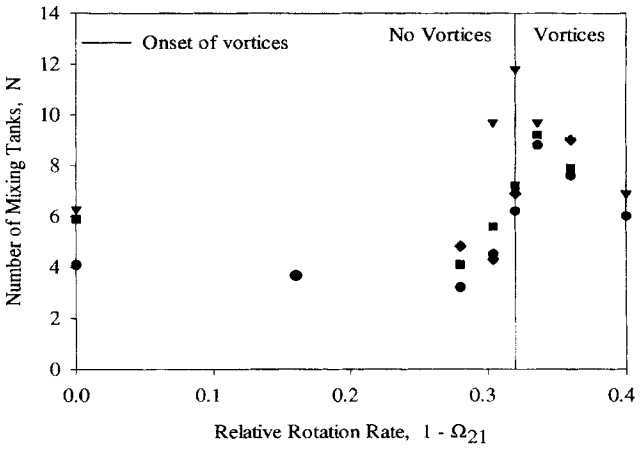

Figure 8. Axial dispersion in the outer fluid with matched viscosity fluids.

The vertical line represents the onset of two-fluid Taylor-Couette flow. The fluids are equal volumes of 60 wt. % glycerine in water and 50 wt. % Drakeol-35 in Isopar-L ($\mu_{21} = 0.96$). The different symbols identify the individual experiment series.

Figure 8 illustrates the effect of Taylor vortices on dispersion in the other phase for the case of nearly matched viscosities—the behavior in the inner phase is essentially identical (Baier, 1999). The minimum axial dispersion occurs in both phases very near the onset of instability. Further increases in the relative rotation rate result in stronger vortices and higher dispersion. This is consistent with similar experiments in the one fluid case.

Figure 9 illustrates the dispersion characteristics of two-fluid Taylor-Couette flow when the phase viscosities are not matched. In this case, the outer fluid is less viscous, and therefore it becomes Rayleigh unstable first. Axial dispersion in the outer fluid is at a minimum (i.e., N is largest) slightly after the outer fluid-critical point. In contrast, the axial dispersion in the inner fluid reaches a minimum after the minimum in the outer phase dispersion but slightly *before* the in-

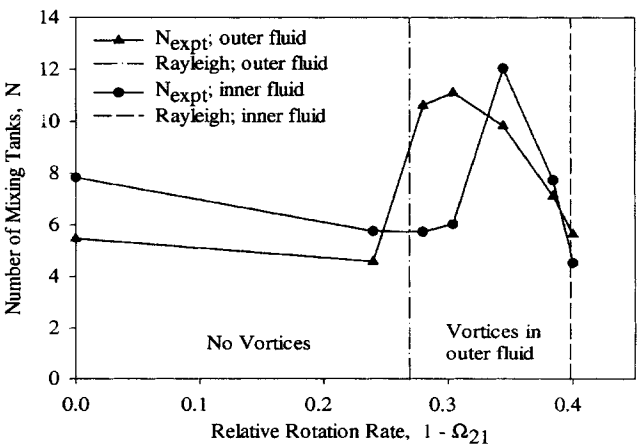

Figure 9. Axial dispersion in both phases with a less viscous outer phase.

Fluid pair 1 in Table 1, $\mu_{21} = 0.63$.

ner fluid critical point (as predicted by the Rayleigh criterion). This occurs because the Rayleigh unstable outer fluid drives a weaker vortex motion in the inner fluid. Similar behavior is observed when the outer fluid is more viscous; again the minimum dispersion occurs first (as $1-\Omega_{21}$ increases) in the first Rayleigh unstable phase, which is now the inner one (Baier, 1999).

The minimum in axial dispersion is consistently observed near the onset of the vortex flow in the corresponding phase. However, the actual quantification of the dispersion is less repeatable. Since dispersion is determined by the shape of the outlet curve, it can be sensitive to small irregularities in the flow pattern and operation. The quantification of axial dispersion in one fluid Taylor-Couette flow also varies widely, although the trends are clear.

Extraction results

The liquid extraction results are based on experiments with the several different tracers and viscosity ratios. The tracers each have a different partition coefficient, m, as identified in Table 2. A comparison of the results for the different tracers reveals which phase tends to be more "mass transfer limiting" for the extraction conditions. The experiments with the different viscosity ratios reveal the effect of vortex strength on extraction performance. Several viscosity ratios were chosen:

1. The nearly matched viscosity case ($\mu_{21} = 0.96$), with both phases Rayleigh unstable and vortices in both phases;

2. The unmatched viscosity case, with only the less viscous phase Rayleigh unstable. Vortices in that phase drive weaker secondary vortices in the more viscous phase. Since the onset of the vortex flow occurs at nearly the same rotation-rate ratio for both experiments ($\mu_{21} = 0.63$, $\mu_{21} = 1.46$), the vortex strengths in both experiments should also be approximately equal.

Results for more extreme viscosity ratios are given in Baier (1999).

The experimental values for the overall mass-transfer coefficients, K_1, were calculated by Eq. 13 using the experimentally determined fraction extracted, f; the effects of axial velocity and dispersion are included in the definition of the mass-transfer coefficient. The values of f are typically reproducible to within $\pm 5\%$. The theoretical predictions for the overall mass-transfer coefficient (neglecting dispersion) were calculated using boundary-layer theory and either (1) the countercurrent axial velocity profile when vortices were not present or (2) CFD of two-fluid Taylor-Couette flow with countercurrent axial flow when vortices were present. The onset of the vortex pattern was determined by the viscous linear stability analysis (Baier and Graham, 1998). Boundary-layer theory predicts the individual mass-transfer coefficients, k_1 and k_2, and the only difference between the two is the diffusivity in that phase. The diffusivity in the outer fluid was estimated by the Wilke-Chang equation as $D_2 = 10^{-6}$ cm^2/s and the diffusivity in the inner fluid as $D_1 = D_2 \mu_{12}$ (Cussler, 1997).

The results for acetophenone ($m = 0.125$) are plotted in Figures 10 (the matched viscosity case) and 11 (the unmatched viscosity cases). Similarly, the results for benzyl alcohol ($m = 14.0$) are in Figures 12 and 13. The onset of vortices in the less viscous phase (as predicted by the inviscid

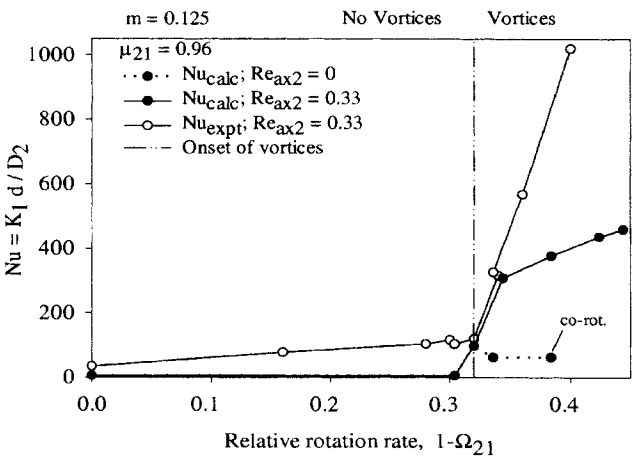

Figure 10. Mass-transfer coefficients for the extraction of acetophenone ($m = 0.125$) from the inner fluid as a function of relative rotation rate.

The matched viscosity case, fluid pair 2.

analysis) is indicated by the vertical lines. There are several important features of these graphs:

- For all cases, the overall mass-transfer coefficient, $Nu = (K_1 d/D_2)$, is small and nearly constant until vortices appear, and then increases dramatically with the increasing strength of the Taylor vortices. The mass-transfer coefficient is approximately linearly proportional to the relative rotation rate as expected by penetration theory and a weakly nonlinear analysis for the vortex velocity strength.
- The calculated mass-transfer performance further increases once the vortices in the more stable phase are sufficiently strong; the slope of the curve (Nu vs. $1-\Omega_{21}$) increases. This point is where corotation first appears when countercurrent axial flow is not present.
- The repeatability of the experiments is good.
- The theoretical predictions and the experimental observations agree within a factor of 3, with the experimental re-

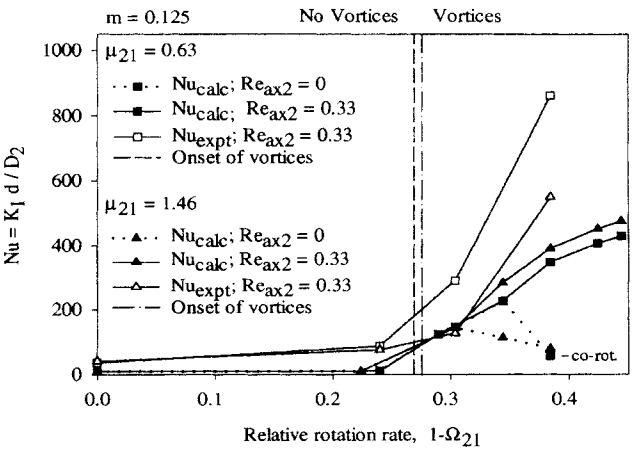

Figure 11. Mass-transfer coefficients for the extraction of acetophenone ($m = 0.125$) from the inner fluid as a function of relative rotation rate.

The unmatched viscosity case, fluid pairs 1 and 3.

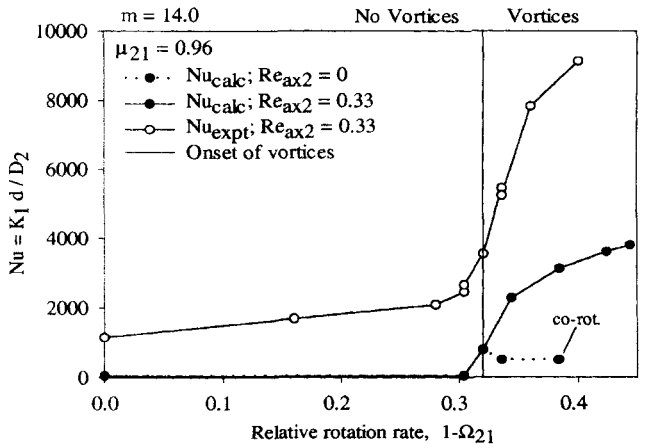

Figure 12. Mass-transfer coefficients for the extraction of benzyl alcohol ($m = 14.0$) from the inner fluid as a function of relative rotation rate.

The matched viscosity case, fluid pair 2.

sults higher than the predictions. The discrepancy is believed to be the increased mixing at the ends. The end effects and axial dispersion were not included in the theoretical analysis.

- The increase in axial dispersion at the higher rotation rates does not seem to degrade the mass-transfer performance. This is not surprising, since the majority of the mass transfer occurs quickly and primarily at the injection end, before dispersion effects develop significantly.
- The maximum Nusselt numbers compare well with those for liquid–liquid extraction in packed columns where correlation for individual mass-transfer coefficients is $Nu_{ind} = 0.0051 Re^{2/3} Sc^{1/2} (ad)^{0.4} [d(g/\nu^2)^{1/3}]$. Here d is the nominal packing size, g is gravity, and the Reynolds number is based on the superficial fluid velocity and the packing area per bed volume a (Cussler, 1997). For $Re = 50$, $Sc = 1{,}000$, $m = 2.7$, and 1-in. Raschig rings, the overall Nusselt number is approximately $Nu = 2{,}000$.

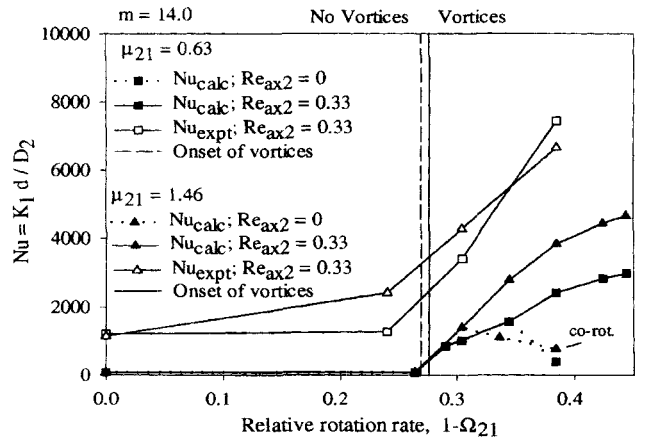

Figure 13. Mass-transfer coefficients for the extraction of benzyl alcohol ($m = 14.0$) from the inner fluid as a function of relative rotation rate.

The unmatched viscosity case, fluid pairs 1 and 3.

Table 3. Comparison of Normalized Overall Mass-Transfer Coefficients as Theoretically Predicted and Experimentally Observed*

Tracer	Partition Coeff., m	$K_{1,norm}$ Theory	$K_{1,norm}$ Exp.
Acetophenone	0.125	1	1
sec-Phenethyl alcohol	2.7	6.6	6.3
Benzyl alcohol	14.0	8.9	9.0

*Sixty wt. % glycerine–water/50 wt. % Drakeol-35 in IsoPar-L ($\mu_{21} = 0.96$).

- When the tracer prefers the raffinate (inner) phase ($m \ll 1$), the extract (outer) phase is "mass transfer limiting." Therefore, Taylor vortices with their higher surface renewal would be expected to be more beneficial in the outer phase. This occurs when the outer fluid is less viscous than the inner fluid ($\mu_{21} < 1$). As observed in Figure 11, the mass-transfer coefficient is always higher when Taylor vortices are in the outer phase. The opposite effect is observed when the tracer prefers the extract (outer) phase, as seen in Figure 13. This suggests the following operating guideline: when $m \gg 1$, better performance is expected when $\mu_{21} > 1$ and vice versa.
- When the Schmidt numbers for the two phases are approximately equal (as in the matched viscosity case), penetration theory predicts that the individual mass-transfer coefficients for the two phases are approximately equal. In this case, the overall mass-transfer coefficient is approximately

$$K_1 = \frac{mk_1}{m+1}. \tag{15}$$

Table 3 shows that the normalized overall mass-transfer coefficients based on Eq. 15 agree well with the experimental values for this matched viscosity case. The theoretical and experimental values were separately normalized by $K_1/K_{1,acetophenone}$.

- Without countercurrent axial flow, FIDAP predicts corotating vortices and a corresponding decrease in mass-transfer performance. Since the experiments do not show a similar decrease, it suggests that corotating vortices have not appeared. Both FIDAP and the linear stability analysis predict that corotating vortices disappear with countercurrent flow (Baier and Graham, 2000).

Only a few experiments were completed at higher countercurrent axial flow rates due to the primitive weir system. As seen in Figure 14, increasing the axial flow rate decreases the mass-transfer performance. This would be expected, since the linear stability analysis with countercurrent flow predicts streamlines bypassing the vortices (Howes and Rudman, 1998; Baier and Graham, 2000). Also, increasing axial flow tends to suppress the instability, and so reduces the vortex strength. The adverse effects of increased flow rate may be counteracted by increasing the relative rotation rate of the cylinders.

The number of theoretical stages can be calculated from Eq. 14, or predicted *a priori* from the CFD-based boundary-layer calculations. Both approaches give approximately 1.5 theoretical stages for the best conditions shown. This is not large, but is quite promising considering that our prototype is far from optimized. Just halving the gap width alone would

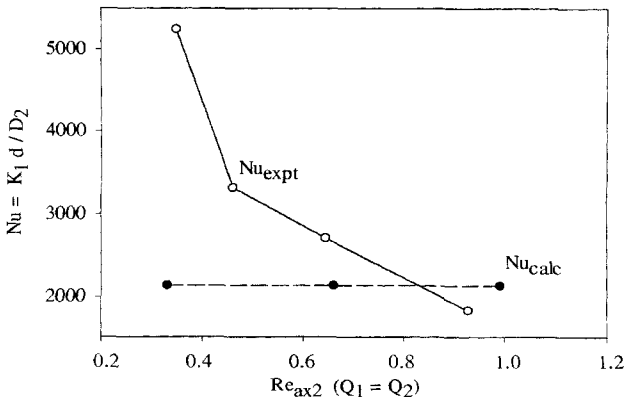

Figure 14. Effect of axial flow rate on the experimentally determined mass-transfer coefficient for the extraction of sec-phenethyl alcohol (m = 2.7) extraction from the inner fluid in the matched viscosity case.

Fluid pair 2.

give twice as many vortices and therefore better mass-transfer coefficients. In addition, modifying the end effects that result from the primitive weir system could also significantly improve the extraction performance and permit operation at larger rotation-rate differences for even higher efficiencies.

These simple modifications would bring us to about the level of available radial liquid extractors, which have benefited from a long optimization process; the Podbielniak centrifugal extractor reports five stages (Cussler, 1997). Our extractor would also be competitive with packed columns for separation efficiency, and with potentially better flow control and decreased product residence times than in packed columns. A major advantage of our extractor remains its simple fluid mechanics and prevention of emulsion formation.

Summary

The present study has demonstrated that two-fluid Taylor-Couette flow with countercurrent axial flow is achievable in practice. When the vortices first appear, axial dispersion decreases and the interphase mass transfer starts to increase. In supercritial two-fluid Taylor-Couette flow, the extraction performance continues to improve with the mass-transfer coefficient proportional to the strength of Taylor vortices. This suggests that further optimization studies and design improvements can produce a highly competitive extractor for the relatively small production levels typical of the biotechnology industry.

The surprisingly good predictability of equipment performance based on well-established fluid mechanics (Baier and Graham, 1998, 2000), computational fluid dynamics, and a relatively simple boundary-layer theory provides a good basis for improvement of design and operation. It also suggests that this novel device is scalable and can be adapted to a wide range of operating conditions.

It remains to refine our mass-transfer model, with increased emphasis on axial dispersion and feed/withdrawal ports, and to construct a second-generation device that profits from the experience obtained with the prototype.

Acknowledgments

This work has been supported by the National Science Foundation under a CAREER award to one of the authors (M.D.G.), the Shell Foundation, and the US-Israel Binational Science Foundation.

Literature Cited

Abbott, N. L., and T. A. Hatton, "Liquid-Liquid Extraction for Protein Separations," *Chem. Eng. Prog.*, 31 (1988).

Acrivos, A., "On the Solution of the Convection Equation in Boundary Layer Flows," *Chem. Eng. Sci.*, **17**, 457 (1962).

Aris, R., "On the Dispersion of a Solute in a Fluid Flowing Through a Tube," *Proc. Roy. Soc. Lond. A*, **237**, 67 (1956).

Baier, G., and M. D. Graham, "Two-Fluid Taylor-Couette Flow: Experiments and Linear Theory for Immiscible Liquids Between Corotating Cylinders," *Phys. Fluids*, **10**, 3045 (1998).

Baier, G., T. M. Grateful, M. D. Graham, and E. N. Lightfoot, "Prediction of Mass Transfer in Spatially Periodic Systems," *Chem. Eng. Sci.*, **54**, 343 (1999).

Baier, G. *Liquid-Liquid Extraction Based on a New Flow Pattern: Two-Fluid Taylor-Couette Flow*, PhD Thesis (Chemical Engineering), Univ. of Wisconsin, Madison (1999).

Baier, G., and M. D. Graham, "Two-Fluid Taylor-Couette Flow: Experiments and Linear Theory for Immiscible Liquids Between Corotating Cylinders with Countercurrent Axial Flow," *Phys. Fluids*, **12**, 294 (2000).

Belfort, G., J. M. Pimbley, A. Greiner, and K.-Y. Chung, "Diagnosis of Membrane Fouling Using Rotating Annular Filter 1. Cell Culture Media," *J. Memb. Sci.*, **77**, 1 (1993a).

Belfort, G., P. Mikulasek, J. M. Pimbley, and K.-Y. Chung, "Diagnosis of Membrane Fouling Using Rotating Annular Filter 2. Dilute Particle Suspensions of Known Particle Size," *J. Memb. Sci.*, **77**, 23 (1993b).

Brenner, H., "Dispersion Resulting from Flow Through Spatially Periodic Porous Media," *Philos. Trans. R. Soc. Lond. A*, **297**, 81 (1980).

Chandrasekhar, S., *Hydrodynamic and Hydromagnetic Stability*, Dover, New York (1981).

Coeuret, F., and J. Legrand, "Mass Transfer at the Electrodes of Concentric Cylindrical Reactors Combining Axial Flow and Rotation of the Inner Cylinder," *Electrochim. Acta*, **26**, 865 (1981).

Cohen, S., and D. M. Marom, "Experimental and Theoretical Study of a Rotating Annular Flow Reactor," *Chem. Eng. J.*, **27**, 87 (1983).

Cussler, E., *Diffusion: Mass Transfer in Fluid Systems*, Cambridge Univ. Press, Cambridge (1997).

Davey, A., "The Growth of Taylor Vortices in Flow Between Rotating Cylinders," *J. Fluid Mech.*, **14**, 336 (1962).

Desmet, G., H. Verelst, and G. V. Baron, "Local and Global Dispersion Effects in Couette-Taylor Flow: I. Description and Modeling of the Dispersion Effects," *Chem. Eng. Sci.*, **51**, 1287 (1996a).

Desmet, G., H. Verelst, and G. V. Baron, "Local and Global Dispersion Effects in Couette-Taylor Flow: II. Quantative Measurements and Discussion of the Reactor Performance," *Chem. Eng. Sci.*, **51**, 1299 (1996b).

Drazin, P. G., and W. H. Reid, *Hydrodynamic Stability*, Cambridge Univ. Press, Cambridge (1981).

Eisenberg, M., C. W. Tobias, and C. R. Wilke, "Mass Transfer at Rotating Cylinders," *Chem. Eng. Prog. Symp. Ser.*, **51**, 1 (1955).

Enokida, Y., K. Nakata, and A. Suzuki, "Axial Turbulent Diffusion in Fluid Between Rotating Coaxial Cylinders," *AIChE J.*, **35**, 1211 (1989).

Flower, J. R., N. Macleod, and A. P. Shahbenderian, "The Radial Transfer of Mass and Momentum in an Axial Fluid Stream Between Coaxial Rotating Cylinders: I. Experimental Measurements," *Chem. Eng. Sci.*, **24**, 637 (1969).

Flower, J. R., and N. Macleod, "The Radial Transfer of Mass and Momentum in an Axial Fluid Stream Between Coaxial Rotating Cylinders: II. The Analogy Between Mass and Momentum Transfer in Streams Containing Secondary Flows," *Chem. Eng. Sci.*, **24**, 651 (1969).

Gehlert, G., S. Luque, and G. Belfort, "Comparison of Ultra- and Microfiltration in the Presence and Absence of Secondary Flow with Polysaccharides, Proteins, and Yeast Suspensions," *Biotechnol. Prog.*, **14**, 931 (1999).

Giordano, R. C., R. L. C. Giordano, D. M. F. Prazeres, and C. L. Cooney, "Analysis of a Taylor-Poiseulle Vortex Flow Reactor—I: Flow Patterns and Mass Transfer Characteristics," *Chem. Eng. Sci.*, **53**, 3635 (1998).

Grifoll, J., X. Farriol, and F. Giralt, "Mass Transfer at Smooth and Rough Surfaces in a Circular Couette Flow," *Int. J. Heat Mass Transfer*, **29**, 1911 (1986).

Gu, Z. H., and T. Z. Fahidy, "Mass Transport in the Taylor-Vortex Regime of Rotating Flow," *Chem. Eng. Sci.*, **40**, 1145 (1985).

Holeschovsky, U. B., and C. L. Cooney, "Quantitative Description of Ultrafiltration in a Rotational Filtration Device," *AIChE J.*, **37**, 1219 (1991).

Howes, T., and M. Rudman, "Flow and Axial Dispersion Simulation for Travelling Axisymmetric Taylor Vortices," *AIChE J.*, **44**, 255 (1998).

Iosilevskii, G., H. Brenner, C. M. V. Moore, and C. L. Cooney, "Mass Transport and Chemical Reaction in Taylor Vortex Flows with Entrained Catalyst Particles: Applications to a Novel Class of Immobilized Enzyme Biochemical Reactors," *Philos. Trans. R. Soc. Lond. A*, **345**, 259 (1993).

Janes, D. A., N. H. Thomas, and J. A. Callow, "Demonstration of a Bubble Free Annular Vortex Membrane Bioreactor for Batch Culture of Red Beet Cells," *Biotechnol. Tech.*, **1**, 257 (1987).

Kappesser, R., I. Cornet, and R. Greif, "Mass Transfer to a Rough Rotating Cylinder," *Electrochem. Soc.*, **118**, 1957 (1971).

Kataoka, K., H. Doi, T. Hongo, and M. Futagawa, "Ideal Plug-Flow Properties of Taylor Vortex Flow," *J. Chem. Jpn.*, **8**, 472 (1975).

Kataoka, K., and T. Takigawa, "Intermixing Over Cell Boundary Between Taylor Vortices," *AIChE J.*, **27**, 504 (1981).

Kawase, Y., and J. J. Ulbrecht, "Laminar Mass Transfer Between Concentric Rotating Cylinders in the Presence of Taylor Vortices," *Electrochim. Acta*, **33**, 199 (1988).

Koschmieder, E. L., "Taylor Vortices Between Eccentric Cylinders," *Phys. Fluids*, **19**, 1 (1976).

Kroner, K. H., V. Nissinen, and H. Ziegler, "Improved Dynamic Filtration of Microbial Suspensions," *Biotechniques*, **5**, 921 (1987).

Kroner, K. H., and V. Nissinen, "Dynamic Filtration of Microbial Suspensions Using an Axially Rotating Filter," *J. Memb. Sci.*, **36**, 85 (1988).

Legrand, J., P. Dumargue, and F. Coeuret, "Overall Mass Transfer to the Rotating Inner Electrode of a Concentric Cylindrical Reactor with Axial Flow," *Electrochim. Acta*, **25**, 669 (1980).

Levenspiel, O., *Chemical Reaction Engineering*, 2nd ed., Wiley, New York (1972).

Lightfoot, E. N., "Estimation of Heat and Mass Transfer Rates," *Lectures in Transport Phenomena*, AIChE Continuing Educ. Ser. No. 4 (1969).

Lo, T. C., M. H. I. Baird, and C. Hanson, *Handbook of Solvent Extraction*, Wiley, New York (1983).

Macleod, N., and T. Ruess, "The Radial Transfer of Mass to an Axial Stream of Liquid Between Coaxial Rotating Cylinders," *Chem. Eng. Sci.*, **30**, 235 (1975).

Moore, C., and C. Cooney, "Axial Dispersion in Taylor-Couette Flow," *AIChE J.*, **41**, 723 (1995).

Murase, T., E. Iritani, P. Chidphong, K. Kano, K. Atsumi, and M. Shirato, "High-Speed Microfiltration Using a Rotating Cylindrical Ceramic Membrane," *Int. Chem. Eng.*, **31**, 370 (1991).

Ohmura, N., K. Kataoka, Y. Shibata, and T. Makino, "Effective Mass Diffusion Over Cell Boundaries in a Taylor-Couette Flow System," *Chem. Eng. Sci.*, **52**, 1757 (1997).

Pudijiono, P. I., N. S. Tavare, J. Garside, and K. D. P. Nigam, "Residence Time Distribution from a Continuous Couette Flow Device," *Chem. Eng. J.*, **48**, 101 (1992).

Pudijiono, P. I., and N. S. Tavare, "Residence Time Distribution Analysis from a Continuous Couette Flow Device Around Critical Taylor Number," *Can. J. Chem. Eng.*, **71**, 312 (1993).

Rosenbluth, M. N., H. L. Berk, I. Doxas, and W. Horton, "Effective Diffusion in Laminar Convective Flows," *Phys. Fluids*, **30**, 2636 (1987).

Schechowskii, J. G., C. A. Koval, and R. D. Noble, "A Taylor Vortex Reactor for Heterogeneous Photocatalysis," *Chem. Eng. Sci.*, **50**, 3163 (1995).

Simmers, D. A., and J. E. R. Coney, "A Reynolds Analogy Solution for the Heat Transfer Characteristics of Combined Taylor Vortex and Axial Flows," *Int. J. Heat Mass Transfer*, **22**, 679 (1979).

Stewart, W. E., "Forced Convection in 3-D Flows: I. Asymptotic Solutions for Fixed Interfaces," *AIChE J.*, **9**, 528 (1963).

Strong, A. B., and L. Carlucci, "An Experimental Study of Mass Transfer in Rotating Couette Flow with Low Axial Reynolds Number," *Can. J. Chem. Eng.*, **54**, 295 (1976).

Tam, W., and H. Swinney, "Mass Transport in Turbulent Couette-Taylor Flow," *Phys. Rev. A*, **36**(3), 1374 (1987).

Taylor, G. I., "Stability of a Viscous Liquid Contained Between Two Rotating Cylinders," *Philos. Trans. R. Soc. Lond. A*, **223**, 289 (1923).

Taylor, G. I., "Dispersion of Soluble Matter in Solvent Flowing Slowly Through a Tube," *Proc. R. Soc. Lond. A*, **219**, 186 (1953).

Toya, Y., and I. Nakamura, "Instability of Two-Fluid Taylor Vortex Flow," *Trans. Jpn. Soc. Mech. Eng. Part B*, **63**, 35 (1997).

Treybal, R. E., *Liquid Extraction*, McGraw-Hill, New York (1963).

Versteegen, P. L., and D. F. Jankowski, "Experiments on the Stability of Viscous Flow Between Eccentric Rotating Cylinders," *Phys. Fluids*, **12**, 1138 (1969).

Winzeler, H., and G. Belfort, "Enhanced Performance for Pressure-Driven Membrane Processes: The Argument for Fluid Instabilities," *J. Memb. Sci.*, **80**, 35 (1993).

Manuscript received Aug. 23, 1999, and revision received May 18, 2000.